High-Performance Transition Metal Dichalcogenide Photodetectors Enhanced by Self-Assembled Monolayer Doping

*Dong-Ho Kang, Myung-Soo Kim, Jaewoo Shim, Jeaho Jeon, Hyung-Youl Park, Woo-Shik Jung, Hyun-Yong Yu, Chang-Hyun Pang, Sungjoo Lee, and Jin-Hong Park**

Most doping research into transition metal dichalcogenides (TMDs) has been mainly focused on the improvement of electronic device performance. Here, the effect of self-assembled monolayer (SAM)-based doping on the performance of WSe_2- and MoS_2-based transistors and photodetectors is investigated. The achieved doping concentrations are $\approx 1.4 \times 10^{11}$ for octadecyltrichlorosilane (OTS) p-doping and $\approx 10^{11}$ for aminopropyltriethoxysilane (APTES) n-doping (nondegenerate). Using this SAM doping technique, the field-effect mobility is increased from 32.58 to 168.9 $cm^2 V^{-1} s$ in OTS/WSe_2 transistors and from 28.75 to 142.2 $cm^2 V^{-1} s$ in APTES/MoS_2 transistors. For the photodetectors, the responsivity is improved by a factor of ≈28.2 (from 517.2 to 1.45×10^4 A W^{-1}) in the OTS/WSe_2 devices and by a factor of ≈26.4 (from 219 to 5.75×10^3 A W^{-1}) in the APTES/MoS_2 devices. The enhanced photoresponsivity values are much higher than that of the previously reported TMD photodetectors. The detectivity enhancement is ≈26.6-fold in the OTS/WSe_2 devices and ≈24.5-fold in the APTES/MoS_2 devices and is caused by the increased photocurrent and maintained dark current after doping. The optoelectronic performance is also investigated with different optical powers and the air-exposure times. This doping study performed on TMD devices will play a significant role for optimizing the performance of future TMD-based electronic/optoelectronic applications.

1. Introduction

2D semiconducting layered transition metal dichalcogenides (TMDs), such as tungsten diselenide (WSe_2), molybdenum disulfide (MoS_2), tungsten disulfide (WS_2), molybdenum diselenide ($MoSe_2$), and hafnium disulfide (HfS_2), have recently become spotlighted as nanomaterials for future flexible, wearable and transparent[1–5] electronic and optoelectronic devices due to their superior physical,[6,7] electrical,[8–10] and optical[11–13] properties. Because of their van der Waals epitaxial structure without dangling bonds, TMD-based electronic devices are immune to short-channel effects and have been considered for next-generation integrated circuits (ICs) with ultrashort channel transistors (below 100 nm).[9] In particular, TMDs are the best materials for optoelectronic applications (e.g., photodetectors[11–13] and solar cells[14,15] due to their tunable energy bandgap properties, which can be controlled by changing their number of layers (from 1.8 to 1.2 eV), and their excellent quantum efficiency.[14,15] Lopez-Sanchez et al.[11] reported a single-layer MoS_2 photodetector with very high photoresponsivity (≈880 A W^{-1}). Lee et al.[12] and Choi et al.[13] also reported multilayer MoS_2 phototransistors with excellent photoresponsivity (≈100 mA W^{-1}).

Meanwhile, the development of doping techniques for 2D TMDs is required to reduce the metal–semiconductor (M-S) contact resistance and also to lower the recombination rate of carriers, which should lead to improved performance of TMD-based electronic and optoelectronic devices. However, recent doping studies have mainly focused on improving the electronic device performance (e.g., the field-effect mobility and contact resistance).

D.-H. Kang, M.-S. Kim, J. Shim, H.-Y. Park, Prof. J.-H. Park
School of Electronics and Electrical Engineering
Sungkyunkwan University
Suwon 440-746, South Korea
E-mail: jhpark9@skku.edu

J. Jeon, Prof. S. Lee
School of Electronics and Electrical Engineering
SKKU Advanced Institute of Nanotechnology (SAINT)
Center for Human Interface Nanotechnology (HINT)
Sungkyunkwan University
Suwon 440-746, South Korea

Dr. W.-S. Jung
Department of Electrical Engineering
Stanford University
CA 94305, USA

Prof. H.-Y. Yu
School of Electrical Engineering
Korea University
Seoul 136-701, South Korea

Prof. C.-H. Pang
School of Chemical Engineering
Sungkyunkwan University
Suwon 440-746, South Korea

DOI: 10.1002/adfm.201501170

Here, we demonstrate a high-performance TMD-based photodetector enhanced by self-assembled monolayer (SAM) doping with octadecyltrichlorosilane (OTS) and 3-aminopropyltriethoxysilane (APTES). One of the OTS functional groups ($-CH_3$) has a positive pole, thereby reducing the electron carrier concentration in the OTS-coated TMD, which indicates p-type doping. Conversely, APTES has an amine ($-NH_2$) functional group with a negative pole, which increases the electron carrier concentration and indicates n-type doping. We systematically investigate the OTS and APTES doping phenomena by Raman spectroscopy and electrical measurements (I_D–V_G and I_D–V_D). Then, the effect of doping on the optoelectronic device performance (photoresponsivity and detectivity) is analyzed with photoluminescence (PL) and optical measurements (under exposure to 520, 655, 785, and 850 nm wavelength lasers). Finally, the performance of TMD photodetectors fabricated with SAM doping techniques is examined in detail, with regard to the optical power of the incident laser and the air-stability of the doping.

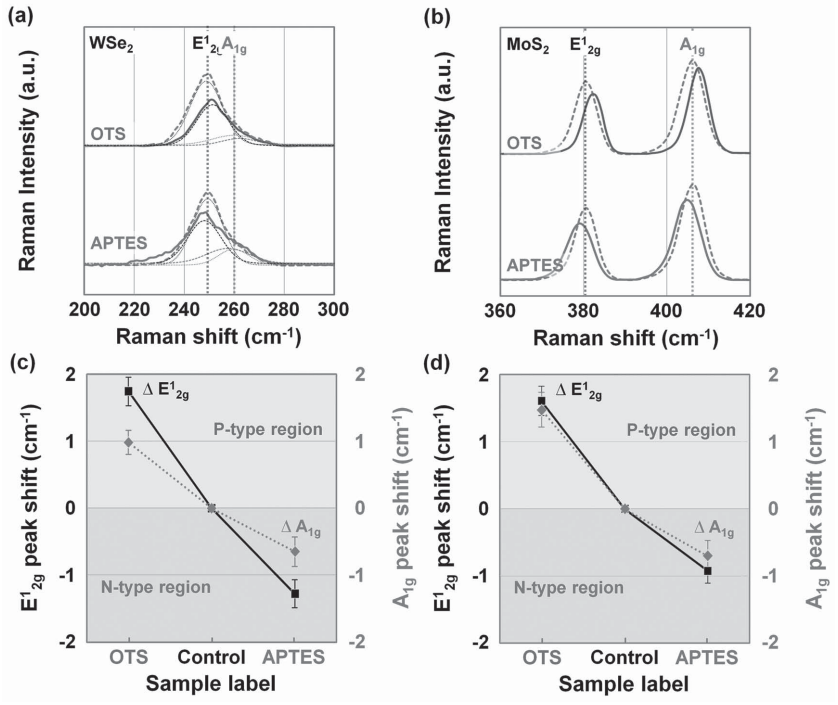

Figure 1. Raman analysis of TMD films doped by OTS or APTES. Raman spectra of OTS- or APTES-doped a) WSe_2 and b) MoS_2. Raman peak shift values of c) WSe_2 and d) MoS_2 doped by OTS or APTES.

2. Result and Discussions

2.1. Raman Analysis of SAM-Doped TMD Films

In order to verify the doping effects of OTS or APTES on TMD films, we performed Raman spectroscopy analysis on OTS or APTES-coated TMD films, where the TMD films were mechanically exfoliated and transferred onto SiO_2/Si substrates. For this Raman analysis, we prepared ten different samples for each doping condition and measured five different points in each sample. **Figure 1**a,b presents the Raman spectra measured on the OTS or APTES-doped WSe_2 and MoS_2 samples, respectively. Although we only found a single peak around ≈250 cm^{-1} on the undoped/doped WSe_2 samples, as shown in Figure S1, Supporting information, two peaks were observed (at 250 and 260 cm^{-1}) on the thin layer WSe_2 films. We then fitted the single Raman peak of WSe_2 with two Gaussian profiles (E^1_{2g} peak at ≈250 cm^{-1} and A_{1g} peak at ≈260 cm^{-1}). For a reference, two different Raman peaks near 250 and 260 cm^{-1} were previously reported on WSe_2 films, which indicate the in-plane (E^1_{2g} peak) and out-plane (A_{1g} peak) vibrations for WSe_2, respectively.[16] The two conventional peaks (E^1_{2g} and A_{1g}) were also observed at ≈380 and ≈406 cm^{-1} in the bulk MoS_2 samples. We then extracted the Raman peak shift values in the two peaks before and after OTS or APTES doping; these values, including error bars, are plotted in Figure 1c,d. In the case of WSe_2, blue-shifting of the Raman peaks was observed after OTS doping, indicating that OTS causes the stiffening of WSe_2 vibrational modes and causes the WSe_2 to become p-doped.[17,18] As shown in Figure 1c, the blue peak shift values caused by OTS p-doping were 1.8 cm^{-1} in E^1_{2g} and 0.98 cm^{-1} in A_{1g}. Alternatively, the E^1_{2g} and A_{1g} peaks were red-shifted in the APTES-coated WSe_2 samples (by –1.3 and –0.74 cm^{-1}, respectively) because APTES caused n-type doping of the WSe_2 films.[19,20] This SAM doping was triggered by the differently charged poles of OTS and APTES. When OTS is coated on WSe_2, the positive poles of OTS accumulate electrons at the interface between OTS and WSe_2, eventually reducing the electron carrier density in WSe_2 (p-type doping).[21] In contrast, APTES has negative poles and pushes electrons away from the interface, which consequently increases the electron carrier density of WSe_2 (n-type doping).[21] The n- and p-type doping phenomena by the SAM layers were also confirmed in MoS_2 samples, as shown in Figure 1d. The blue-shift values of the E^1_{2g} and A_{1g} peaks were 1.8 and 1.7 cm^{-1}, respectively, in OTS-doped MoS_2 samples (p-doping), and red-shifts of –0.9 and –0.8 cm^{-1} were observed in the E^1_{2g} and A_{1g} peaks, respectively, in the case of APTES-doped MoS_2 samples (n-doping).

2.2. Electrical Characteristics of OTS- and APTES-Doped TMD Electronic Devices

To once again confirm the doping effects of OTS and APTES on the TMD materials, we fabricated TMD-based electronics (transistors) and investigated the electrical characteristics of these devices. **Figure 2**a shows the schematic diagram of a SAM-coated TMD back-gate transistor and the energy band diagrams of the metal-undoped/doped TMD junctions under the operating voltage bias. When OTS is coated on the WSe_2 device, positive charges from $-CH_3$ groups in OTS seem to accumulate electron carriers at the interface between OTS and WSe_2 (p-doping),

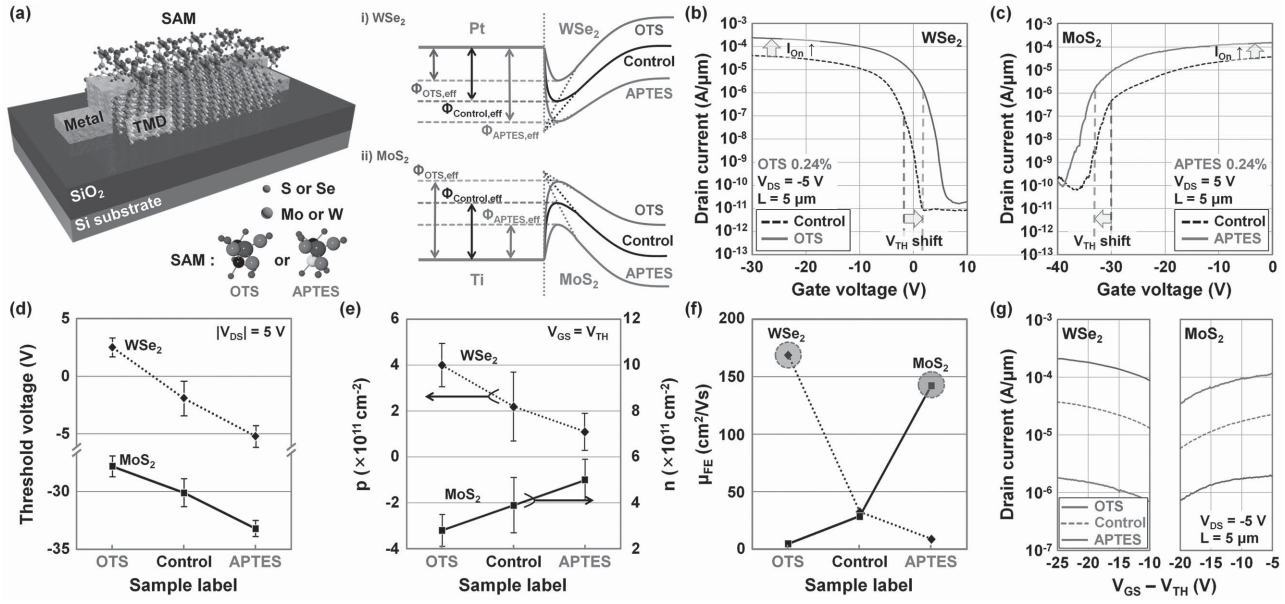

Figure 2. Electrical characterization of TMD transistors doped by OTS or APTES. a) Schematic diagram of the back-gated transistor device fabricated on TMD films doped by OTS or APTES and the energy band diagrams of the source-undoped/doped TMD junctions. The I_D–V_G characteristics of the b) undoped/OTS-doped WSe_2 and c) undoped/APTES-doped MoS_2 transistors. The variations in the d) threshold voltage (V_{TH}), e) carrier concentration (WSe_2: p and MoS_2: n), f) field-effect mobility (μ_{FE}), and g) on-current extracted from the WSe_2 and MoS_2 transistors, which were undoped/doped by OTS or APTES. Here, the I_D was normalized by the channel width (W).

subsequently shifting up the WSe_2 energy band and increasing the electric field at the Pt-WSe_2 junction. This phenomenon consequently reduces the effective barrier height of the Pt-WSe_2 junction, and the threshold voltage is positively shifted by the increased hole injection probability from Pt into the WSe_2 channel (Schottky barrier lowering effect: $\Phi_{Control} > \Phi_{OTS\_eff}$). In contrast, in the case of the APTES-doped WSe_2 device, negative charges from the $–NH_2$ groups in APTES are expected to accumulate hole carriers (n-doping), consequently shifting down the WSe_2 energy band and increasing the effective barrier height of the Pt–WSe_2 junction. As a result, this reduced hole injection probability seems to decrease the V_{TH} value ($\Phi_{Control} < \Phi_{APTES\_eff}$). As shown in the right-bottom of Figure 2a, the opposite phenomenon is predicted in MoS_2 devices; the energy band is shifted-down by APTES n-doping, which helps inject electron carriers into the MoS_2 n-channel ($\Phi_{OTS\_eff} > \Phi_{Control} > \Phi_{APTES\_eff}$ in the MoS_2 device). Figure 2b,c) shows the I_D–V_G characteristics of undoped/OTS-doped WSe_2 and undoped/APTES-doped MoS_2 samples, where the applied V_{DS} values are –5 and 5 V, respectively. In the WSe_2 devices, a positive shift in the V_{TH} (from –2 to 2.4 V) and an increase in the on-current by a factor of 6.6 (from 2.8×10^{-5} to 1.98×10^{-4} A μm^{-1}) were observed after doping with 0.24% OTS; this indicated the p-type doping of WSe_2. After APTES doping on the MoS_2 device, we found a negative shift in the V_{TH} (from –30.1 to –33.6 V) and an on-current enhancement (from 2.2×10^{-5} to 1.08×10^{-4} A μm^{-1}), indicating the n-type doping of MoS_2. As shown in Figure 2d and mentioned above, when OTS was coated on the WSe_2 and MoS_2 devices, a positive shift in the V_{TH} was observed in both samples. This is also consistent with the previous Raman analysis. When APTES was coated on the TMD devices, a negative shift in the V_{TH} was observed in both samples, indicating that APTES caused n-type doping of the TMD (from –2 to –5 V in WSe_2 and from –30.1 to –33.6 V in MoS_2). To compare the doping levels achieved by OTS and APTES, we then calculated the 2D sheet doping concentrations on each SAM-doped TMD sample and plotted the concentration values in Figure 2e. The hole carrier concentration was increased from 2.2×10^{11} to 4.0×10^{11} cm^{-2} ($\Delta p = p_{SAM} - p_{Control} = \approx 1.8 \times 10^{11}$ cm^{-2}) in the WSe_2 device after OTS doping, compared to the control. However, APTES doping decreased the hole concentration from 2.2×10^{11} to 1.1×10^{11} cm^{-2} ($\Delta p = -1.1 \times 10^{11}$ cm^{-2}). In the case of MoS_2, the amount of variance in the electron carrier concentrations after SAM doping were about 1.4×10^{11} cm^{-2} (p-doping by OTS) and -1.0×10^{11} cm^{-2} (n-doping by APTES). The achieved SAM doping level is in the nondegenerate regime, which is similar to that of the recently reported DNA n-doping ($\approx 6.4 \times 10^{10}$ cm^{-2})[19] and Cs_2CO_3 n-doping ($\approx 10^{11}$ cm^{-2}).[20] We also extracted and plotted the field-effect mobility values before/after SAM doping; this difference is shown in Figure 2f. When the WSe_2 device was doped by OTS, the field-effect mobility was increased from 32.58 to 168.9 cm^2 V^{-1} s. This improvement was also observed in the APTES-doped MoS_2 device (increasing from 28.75 to 142.2 cm^2 V^{-1} s). However, the field-effect mobility deteriorated in the APTES-doped WSe_2 (decreasing from 32.58 to 8.98 cm^2 V^{-1} s) and the OTS-doped MoS_2 (decreasing from 28.75 to 4.8 cm^2 V^{-1} s) due to the increased injection barrier height. Similar changes were also observed in the on-currents of the OTS- or APTES-doped TMD devices. As shown in Figure 2g, compared to the control device, the on-current of the OTS-doped WSe_2 device was increased by a factor of ≈6.6 (from 3.06×10^{-5} to 1.8×10^{-4} A) at $V_{GS} - V_{TH} = 20$ V; however, the on-current of the APTES-doped WSe_2 device was reduced by a factor of ≈0.05 from 3.06×10^{-5} to 1.6×10^{-6} A. The on-current

changes in the OTS- or APTES-doped MoS_2 devices showed the opposite trend to the WSe_2 device (OTS: $1.73 \times 10^{-5} \rightarrow 1.74 \times 10^{-6}$ A and APTES: $1.73 \times 10^{-5} \rightarrow 9.63 \times 10^{-5}$ A). This indicates that the barrier lowering effect caused by doping with the same doping type as the carrier type of the channel (OTS doping on WSe_2 or APTES doping on MoS_2) can improve the field-effect mobility and on-current by increasing the carrier injection probability.

2.3. Characterization of OTS- or APTES-Doped TMD Optoelectronic Device

Figure 3a shows the structural schematic diagram for the OTS- or APTES-doped TMD photodetectors. We obtained the optical characteristics of the OTS- or APTES-doped TMD photodetectors, including the current-voltage (I_D–V_G) curves under dark and illuminated conditions (P_{light} = 5.8 mW cm^{-2} and λ = 655 nm); these are plotted in Figure 3b,c. In the OTS-doped WSe_2 and APTES-doped MoS_2 photodetectors (obtained at V_{DS} = −5 and 5 V, respectively), the photocurrents were increased by about 10 times in the off-state (WSe_2: $V_{GS} < V_{TH}$ and MoS_2: $V_{GS} > V_{TH}$). On the contrary, we observed the deterioration of photocurrents in the APTES-doped WSe_2 and OTS-doped MoS_2 photodetectors. This indicates that the SAM doping influenced the performance of the optoelectronic device. The improvement or deterioration was mainly attributed to the type of doping. We then extracted photoresponsivity ($R = I_{Photo}/P_{Light}$) and detectivity ($D^* = (RA^{1/2})/(2eI_{Dark})^{1/2}$) values, as shown in Figure 3d,e. This was done in order to investigate the effect of SAM doping on the optoelectronic device performance in more detail. Here, the generated photocurrent is I_{Laser_on}–I_{Laser_off}, P_{Light} is the total incident optical power, A is the effective area of the device, e is the absolute electron charge value (1.6×10^{-19} C), and I_{Dark} is the dark current. In Figure 3d, the photoresponsivity and detectivity of the OTS-doped WSe_2 device were increased by a factor of ≈17.6 (from 20 to 364 A W^{-1}) and ≈15.2 (from 3.48×10^9 to 5.3×10^{10} Jones), respectively, compared to the control device. However, when APTES was coated on the WSe_2 device (n-doping), the photoresponsivity and detectivity were reduced by a factor of ≈0.03 (from 20 to 0.59 A W^{-1}) and ≈0.09 (from 3.48×10^9 to 3.43×10^8 Jones), respectively. We also note that the photoresponsivity and detectivity were extracted at $V_{GS} = V_{TH}$ and $V_{GS} - V_{TH}$ = 4 V, respectively. Alternatively, the opposite trends for photoresponsivity and detectivity were observed in the case of MoS_2 devices, as shown in Figure 3e. When the MoS_2 device was p-doped by OTS, the photoresponsivity was reduced by a factor of ≈0.08 (from 4.1 to 0.36 A W^{-1}) and the detectivity was lowered by a factor of ≈0.15 (from 3.39×10^8 to 5.3×10^7 Jones). In the APTES-doped MoS_2 photodetector, we observed an improvement in the photoresponsivity and detectivity, which were

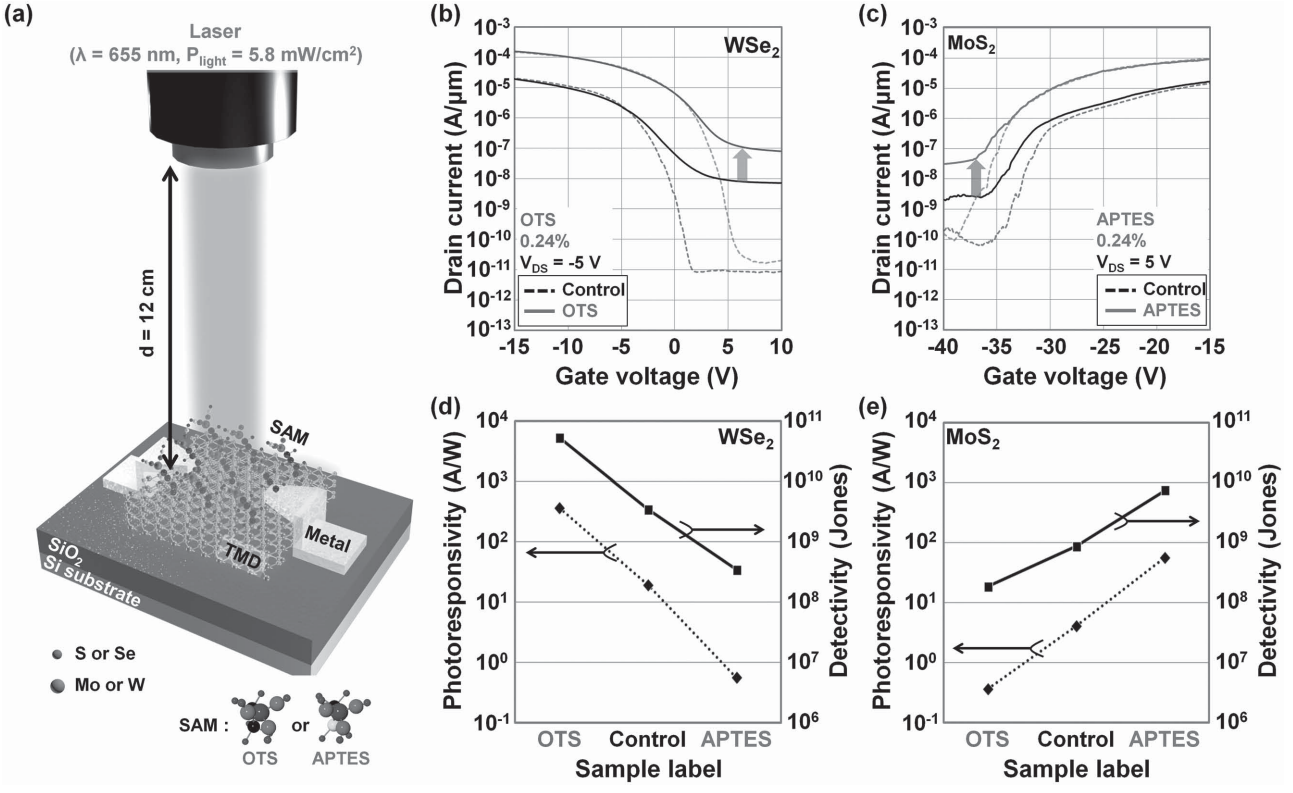

Figure 3. Characterization of TMD photodetectors doped by OTS or APTES. a) Schematic diagram of the back-gated photodetector fabricated on TMD films doped by OTS or APTES under exposure to a light source (λ = 655 nm and P = 5.8 mW cm^{-2}). The I_D–V_G characteristics of the b) undoped/OTS-doped WSe_2 and c) undoped/APTES-doped MoS_2 photodetectors before/after laser exposure. The d) photoresponsivity (R) and e) detectivity (D^*) extracted from the WSe_2 and MoS_2 photodetectors, which were undoped/doped by OTS or APTES. Here, the I_D was also normalized by the channel width (W).

increased by a factor of ≈13.8 and ≈12.6, respectively (up to 56.5 A W^{-1} and 4.47×10^9 Jones). The photoresponsivity values of OTS/WSe_2 and APTES/MoS_2 devices were also plotted as a function of gate voltage in Figure S7, Supporting Information. The maximum photoresponsivity value of OTS/WSe_2 device was 1925.2 A W^{-1} and APTES/MoS_2 device showed 1212.8 A W^{-1}, indicating that photoresponsivity is dependent on the conductivity of channel. Through this optoelectronic device analysis, we clearly confirmed that these significant changes in the device performance were caused by the different type of doping. Furthermore, we investigated the effects of doping level on the photodetector performance (see Figure S9, Supporting Information). The performance of OTS- and APTES-doped WSe_2 photodetectors was respectively enhanced or degraded as SAM doping concentration increased.

The effect of SAM doping on TMD-based photodetector performance (e.g., photoresponsivity or detectivity) seems to originate from the optical properties of the TMD materials. **Figure 4**a shows some schematics explaining the excitation and relaxation mechanisms of electron–hole pairs in i) WSe_2 and ii) MoS_2 materials under illuminated conditions. When a laser with energy greater than 1.85 eV (or below 670 nm) is exposed to WSe_2 and MoS_2, electrons are optically excited from the valance band to the conduction band, consequently forming electron–hole pairs (or excitons). However, since the excited electrons are unstable, they are likely to relax from the conduction band to the valance band. During this relaxation step, the electrons seem to recombine with holes, inducing radiation. As a result, in Figure 4b,c, we observed several photoluminescence (PL) peaks for WSe_2 and MoS_2, respectively. In the case of WSe_2, two peaks appeared near ≈1.63 and ≈1.66 eV, each signifying negatively charged X^- trion (two electrons and one hole) and positively charged X^+ trion (one electron and two holes) peaks. However, an X^0 exciton peak was not clearly observable in the PL spectra because the intensity of X^0 PL peaks is relatively lower than the others. Compared to the control, the X^- peak intensity in the OTS-doped WSe_2 sample was decreased, indicating that the radiative recombination of negatively charged trions was suppressed. This seems to be caused by the fact that the number of negatively charged trions formed by laser exposure was reduced due to the decrease in the electron concentration caused by OTS p-doping.[22] Alternatively, the opposite behavior (an increase in the X^- peak intensity) was observed in the APTES-doped WSe_2 sample (n-doping), indicating that the radiative recombination probability of negatively charged trions was increased. It is believed that the electrons in WSe_2, which are additionally obtained via APTES n-doping, increase the density of negative charged trions.[22] For a reference, Ross et al.[23] previously reported the PL spectra of WSe_2 and showed three conventional peaks that correspond to the negative charged

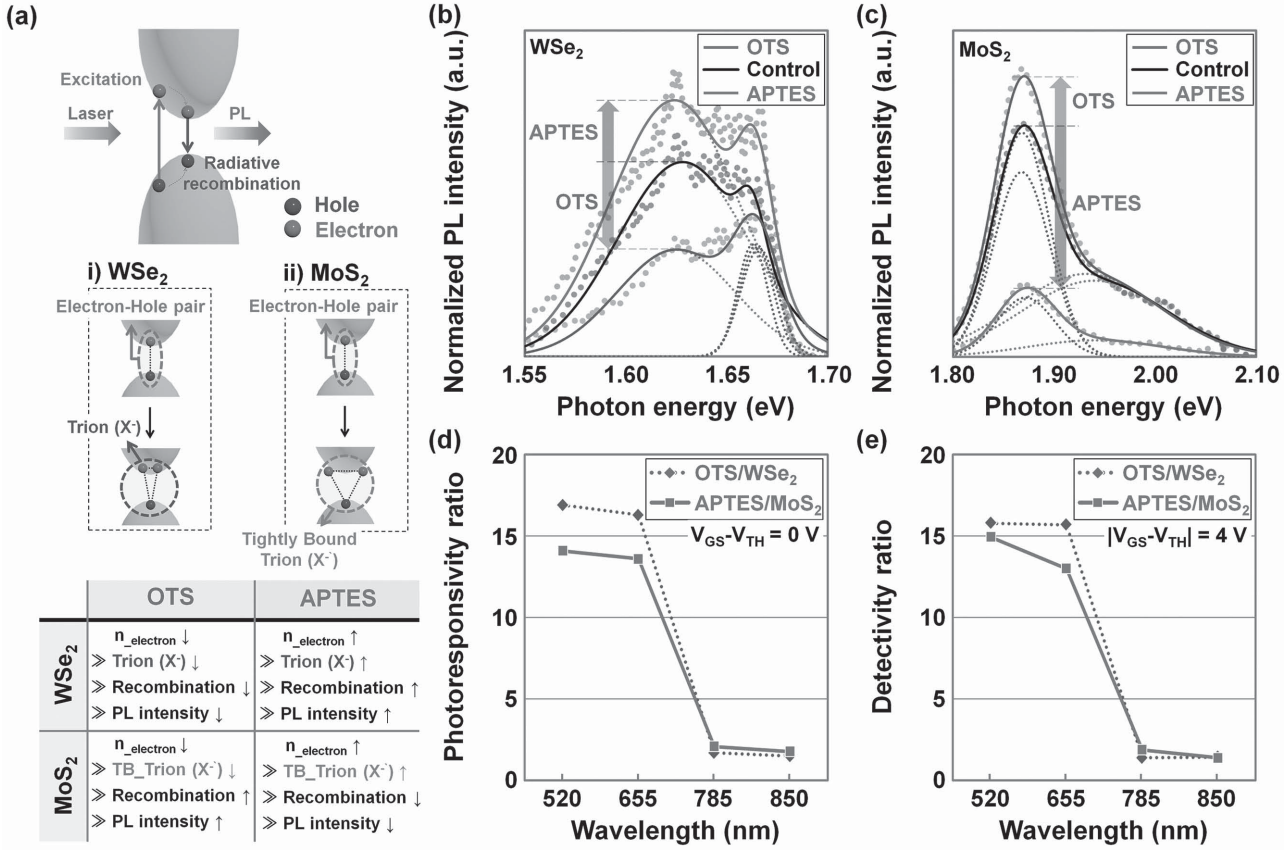

Figure 4. Optical characterization of OTS or APTES doping effects on TMD films. a) Schematic diagram showing the excitation and relaxation mechanisms of electron-hole pairs in TMD films under illumination. The PL spectra of undoped/doped b) WSe_2 and c) MoS_2. The d) photoresponsivity ratio ($R_{\_SAM}/R_{\_Control}$) and e) detectivity ratio ($D^*_{\_SAM}/D^*_{\_Control}$), which were extracted from the OTS-doped WSe_2 and APTES-doped MoS_2 photodetectors under exposure to various laser wavelengths (520, 655, 785, and 850 nm).

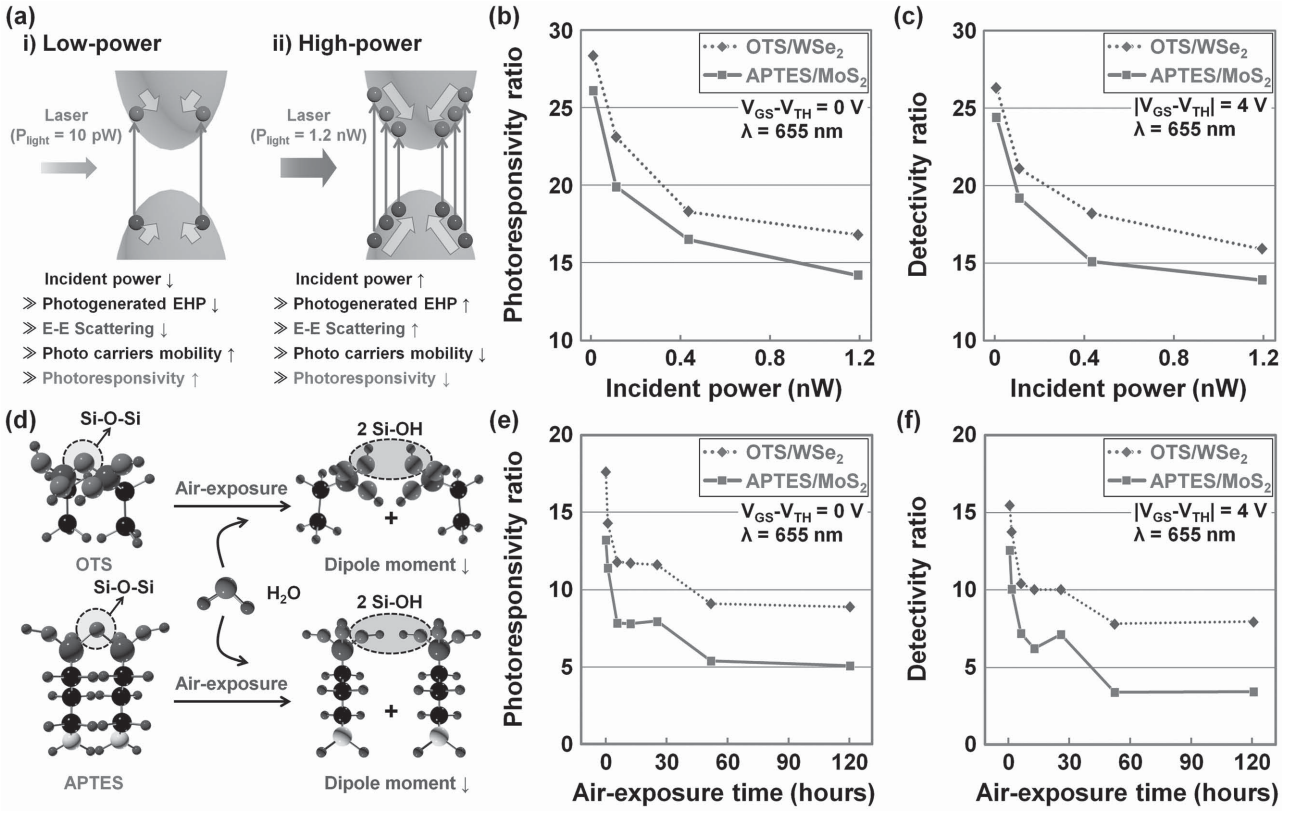

Figure 5. Power-dependence and air-stability of OTS-doped WSe_2 and APTES-doped MoS_2 photodetectors. Schematic diagram showing the a) power-dependence and d) air-stability mechanisms of the OTS- or APTES-doped TMD photodetectors. The photoresponsivity ratio ($R_{\_SAM}/R_{\_Control}$) as a function of the b) optical power and e) air-exposure time. The detectivity ratio ($D^*_{\_SAM}/D^*_{\_Control}$) as a function of the c) optical power and f) air-exposure time.

X^- trion (≈1.625 eV), positive charged X^+ trion (≈1.663 eV), and X^0 exciton (≈1.69 eV).

In the case of MoS_2, two conventional peaks indicating the formation of excitons were observed near 1.92 eV (A exciton) and 2.08 eV (B exciton); these formed due to the spin-orbit splitting at the edge of the valence band.[24] We then fitted the PL spectra in all MoS_2 samples with two peaks (1.92 and 2.07 eV), as shown in Figure 4c. Compared to the control MoS_2 sample, the peak intensities for A and B excitons of the OTS-doped MoS_2 samples were increased, indicating that the probability of excitonic radiative recombination was increased by the OTS p-doping. When the electron concentration is decreased by the OTS p-doping, tightly bound trions are difficult to form and the radiative recombination of excitons increases. Similarly, the PL peak intensity of APTES-doped MoS_2 was decreased because the increased number of tightly bound trions (caused by n-doping) reduced the radiative recombination of excitons.[25] Mak et al.[25] previously reported that the PL intensity of MoS_2 (A and B excitons) is dependent on the formation of tightly bound trions in MoS_2. Overall, in the cases of OTS-doped WSe_2 and APTES-doped MoS_2, PL peak intensities were reduced, indicating that the carrier recombination probability decreased, leading to an increase in the photocurrent, which was caused by the doping effect.[20] We also performed a PL analysis on SAM layers without TMD. Here, we could not observe any peaks because APTES and OTS have a large HOMO-LUMO gap (larger than 2.1 eV), consequently indicating that the PL peaks observed in SAM-doped TMD films were a response caused by MoS_2 layer. On the contrary, the increase in the PL peak intensity of the APTES-doped WSe_2 and OTS-doped MoS_2 samples led to a reduced photocurrent (refer to the Figure 3). In addition, we measured photocurrents after exposing a laser with various wavelengths (520, 655, 785, and 850 nm) to the OTS/WSe_2 and APTES/MoS_2 photodetectors. With this photocurrent data, we then calculated the ratio of photoresponsivity (at $V_{GS} = V_{TH}$) and detectivity ($|V_{GS} - V_{TH}| = 4$ V), as shown in Figure 4d,e. The photoresponsivity (ranging from about 13–17.2) and detectivity (ranging from about 12.6–15.5) were enhanced when a higher energy laser ($\lambda < 670$ nm) was exposed, compared to the case when a lower energy laser with a longer λ above 750 nm was used (photoresponsivity ratio = 1.5–2, detectivity ratio = 1.2–2.1). Based on this observation, it is predicted that the performance enhancement caused by the doping technique is more effective under exposure to higher energy lasers because the absorbing probability through direct transition is improved when a laser with a higher energy is used. For a reference, the direct bandgaps for bulk WSe_2 and MoS_2 (E_{g_MoS2} and E_{g_WSe2}) are known to be ≈1.65[26] and ≈1.85,[27] respectively.

Figure 5 shows the extended analysis of the performance enhancement of SAM-doped TMD photodetectors according to the (a–c) optical power of the incident laser and the (d–f) air-stability of the SAM doping. In general, the photoresponsivity

exponentially increases as the optical power of the laser decreases.[28–30] This is thought to be caused by the scattering phenomenon between photoexcited electrons, as shown in Figure 5a. When a low power laser is exposed to photodetectors, the amount of photogenerated carriers is decreased. In this case, the mobility of the carriers seems to increase due to the suppressed scattering, which consequently increases the photoresponsivity under exposure to a low power laser.[30] This phenomenon was also confirmed in our OTS/WSe_2 and APTES/MoS_2 photodetectors through the photoresponsivity measurement with various incident powers (10, 170, 420, and 1200 pW). The maximum photoresponsivity values of undoped WSe_2 and MoS_2 photodetectors were 517.2 and 219.3 A W^{-1}, respectively. After SAM doping (OTS for WSe_2 and APTES for MoS_2), the photoresponsivity ratio ($R_{SAM}/R_{Control}$) was dramatically increased by a factor of ≈28.2 (R varied from 517.2 to 1.45×10^4 A W^{-1}) in the OTS/WSe_2 device and ≈26.4 (R varied from 219 to 5.75×10^3 A W^{-1}) in APTES/MoS_2, as the incident laser power was lowered. This improvement in photoresponsivity is much larger compared to other approaches that have been used to enhance the performance of MoS_2 photodetectors, such as using R6G[31] as an additional absorber (≈11.2-fold increase in photoresponsivity) or applying the n-doping technique with Cs_2CO_3[20] (≈5-fold increase in photoresponsivity). In addition, the enhanced photoresponsivity values were much higher than that of the previously reported TMD photodetectors.[11–13,31] Similarly, enhanced detectivity was also observed upon exposure to a laser with a lower power (from a 15.2-fold increase to a 26.6-fold increase in the OTS/WSe_2 device and from a 12.6-fold increase to a 24.5-fold increase in the APTES/MoS_2 device) due to the unchanged off-current level caused by the low-level doping process (for a reference, $D^* \propto R/I_{Dark}^{1/2}$).

In addition, we monitored the air-stability of the OTS and APTES doping effects on TMD photodetectors. Figure 5d shows the schematic diagrams of the OTS and APTES doping deterioration mechanisms during exposure to air. When OTS is exposed to air, the –$SiCl_3$ functional groups immediately react with moisture in the air to form $Si(OH)_3$. After an annealing process at ≈120 °C, the –OH groups are expected to react with other –OH groups to form Si–O–Si bonds, consequently strengthening the p-doping effect (increasing the dipole moment). However, these Si–O–Si bonds seems to be easily broken by H_2O and return to Si–OH bonds after long exposure to air.[18] A similar mechanism is also expected to occur in the case of APTES doping; the tail group of APTES easily reacts with H_2O to form $Si(OH)_3$ bonds.[32] The FT-IR data obtained on the APTES-doped TMD samples can be seen in Figure S6, Supporting Information. After 7 d in air, Si–OH bond peak (≈880 cm^{-1}) newly emerged and Si–O–Si bond peak (≈1030 and ≈1080 cm^{-1}) decreased, indicating that the Si–O–Si bonds were broken through the reaction with H_2O (forming Si–$(OH)_3$ bonds). The stability of photodetector performance (photoresponsivity and detectivity ratio) was investigated in Figure 5e,f. After air exposure for 6 h, the photoresponsivity ratios of the OTS/WSe_2 and APTES/MoS_2 samples were decreased by about 33% (from 17.6 to 11.8 in the OTS/WSe_2 device and from 13.8 to 7.9 in the APTES/MoS_2 device). These values were eventually reduced by 48%–63% after 120 h (from 17.6 to 9.1 in the OTS/WSe_2 and from 13.8 to 5.1 in the APTES/MoS_2). The deterioration of the detectivity ratio (50%–69% reduction after 120 h) also showed a similar tendency with the trend in photoresponsivity in both the OTS/WSe_2 and APTES/MoS_2 devices.

3. Conclusion

In conclusion, we demonstrated the SAM doping effect on the performance of TMD photodetectors with Raman spectroscopy, PL, and electrical and optical measurements. The performance was investigated in terms of the photoresponsivity and detectivity as the incident optical powers and the air-exposure times were varied. The doping concentrations achieved for TMDs were between 1.4×10^{11} and 1.8×10^{11} cm^{-2} for p-doping by OTS and between 10^{11} and 1.1×10^{11} cm^{-2} for n-doping by APTES. When the WSe_2-based transistor was doped by OTS, its field-effect mobility was increased from 32.58 to 168.9 cm^2 V^{-1} s. A similar increase was also observed in the APTES-doped MoS_2-based transistor (from 28.75 to 142.2 cm^2 V^{-1} s). However, the field-effect mobilities were deteriorated in the APTES-doped WSe_2 and the OTS-doped MoS_2 due to the increased injection barrier height. In the case of OTS-doped WSe_2 and APTES-doped MoS_2 photodetectors, the photoresponsivity, and detectivity were increased 13.8–17.6 times and 12.6–15.2 times, respectively, compared to the control (undoped), thereby achieving 364 A W^{-1}/5.3×10^{10} Jones for the WSe_2 device and 56.5 A W^{-1}/4.47×10^9 Jones for the MoS_2 device. Alternatively, the opposite trend was observed in the photoresponsivity and detectivity of the APTES-doped WSe_2 and OTS-doped MoS_2 devices. This effect of SAM doping on the TMD-based photodetector performance originated from the optical properties of the TMD materials. In the case of WSe_2, the X^- peak intensity was decreased (compared to the control), indicating that the radiative recombination of negatively charged trions was suppressed. This was due to the fact that the number of negatively charged trions was reduced by the decrease of the electron concentration caused by OTS p-doping. Alternatively, the opposite behavior (an increase in the X^- peak intensity) was observed in the APTES-doped WSe_2 sample (n-doping), demonstrating that the radiative recombination probability of negatively charged trions was increased by the electrons obtained through APTES n-doping. In the case of OTS-doped MoS_2, the peak intensities for A and B excitons were increased, indicating that the probability of radiative recombination by excitons was relatively increased by the OTS p-doping. This is because tightly bound trions were hardly formed due to the reduced number of electrons caused by the p-doping. Similarly, the PL peak intensity of APTES-doped MoS_2 was decreased by the increased number of tightly bound trions that was caused by n-doping, reducing the radiative recombination of excitons. Overall, in the OTS-doped WSe_2 and APTES-doped MoS_2, the PL peak intensities were reduced, indicating that the recombination probability of carriers decreased. This led to an increase in the photocurrent in the OTS-doped WSe_2 and APTES-doped MoS_2 photodetectors. On the contrary, an increase in the PL peak intensity of the APTES-doped WSe_2 and OTS-doped MoS_2 samples led to a reduction of the photocurrent. In addition, we also confirmed that the performance enhancement obtained by doping is more

effective under exposure to higher energy lasers because the absorbing probability through direct transition is improved when a laser has a higher energy ($\lambda < 670$ nm). We also investigated the performance enhancement of SAM-doped TMD photodetectors in terms of the optical power of the incident laser and the air-stability of the SAM doping. When a low power laser was exposed to the OTS/WSe_2 and APTES/MoS_2 photodetectors, the photoresponsivity and detectivity dramatically increased because the mobility of the photogenerated carriers increased due to suppressed scattering. After SAM doping, the photoresponsivity ratio was increased by a factor of ≈28.2 (R varied from 517.2 to 1.45×10^4 A W^{-1}) in the OTS/WSe_2 device and ≈26.4 (R varied from 219 to 5.75×10^3 A W^{-1}) in APTES/MoS_2, as the power of the incident laser was lowered. The improved photoresponsivity values were much higher, compared to that of the previous TMD-based photodetectors. Similarly, enhanced detectivity was also observed upon exposure to a laser with a lower power (from a 15.2-fold increase to a 26.6-fold increase in the OTS/WSe_2 device and from a 12.6-fold increase to a 24.5-fold increase in the APTES/MoS_2 device) due to the unchanged off-current level caused by the low-level doping process. Finally, we monitored the effect of OTS and APTES doping on the air-stability of TMD photodetectors. After an annealing process at ≈120 °C, –OH groups are expected to react with other –OH groups to form Si–O–Si bonds, consequently strengthening the p-doping effect (increasing dipole moment). However, these Si–O–Si bonds seem to be easily broken by H_2O and return to Si–OH bonds after long exposure to air. A similar mechanism is also predicted to occur in the case of APTES doping; the tail group of APTES easily react with H_2O to form $Si(OH)_3$ bonds. After air exposure for 6 h, the photoresponsivity ratios of the OTS/WSe_2 and APTES/MoS_2 devices were decreased by about 33% and were eventually reduced by 48%–63% after 120 h. The deterioration of the detectivity ratio (50%–69% reduction after 120 h) also showed a similar tendency with the trend in photoresponsivity in both the OTS/WSe_2 and APTES/MoS_2 devices. Overall, appropriate SAM doping (OTS for WSe_2 and APTES for MoS_2) plays a significant role in the performance improvements of TMD-based optoelectronic devices.

4. Experimental Section

Formation of OTS and APTES Doping on TMD Films: WSe_2 and MoS_2 flakes were mechanically exfoliated onto a 90 nm thick dry-oxidized SiO_2 layer grown on a heavily doped p-type Si substrate (resistivity < 0.005 Ω m) by tape. Here, TMD flakes with similar thickness (≈27.7 nm for WSe_2 and ≈23.7 nm for MoS_2) were selected through atomic force microscopy (AFM) analysis in order to avoid thickness effects (Figure S2, Supporting Information). To form OTS and APTES layers on the TMD samples, 120 µL of OTS and APTES were added to 50 mL of hexane (a mixture of isomers) and toluene, respectively. Then, the TMD samples were soaked in each solution for 1 h. Next, the samples were rinsed several times with toluene, acetone, and deionized water and baked at 120 °C for 20 min in a vacuum (Figure S3, Supporting Information).

Characterizations of OTS- or APTES-Doped TMD Films: OTS- or APTES-doped TMD samples were investigated and compared with a control sample (undoped TMD) by PL/Raman spectroscopy (Alpha300 M+, WITec) at room temperature (Raman) and 200 K (PL). Here, the wavelength and power of the incident laser were 532 nm and 2 mW, respectively. The beam size of the laser used for the Raman and photoluminescence analyses was approximately 0.7–0.9 µm, and the instrumental spectral resolution was less than 0.9 cm^{-1}. The gratings of the spectrometer were set at 1800 and 600 g mm^{-1} for the Raman spectra and PL measurements, respectively.

Fabrication of OTS- or APTES-Doped TMD Electronic/Optoelectronic Devices: For the fabrication of back-gated TMD transistors, we patterned source/drain electrode regions (channel length and width are 5 µm) on TMD/SiO_2/Si samples by optical lithography, followed by the deposition of 10 nm thick Ti (for MoS_2) or Pt (for WSe_2) and 50 nm thick Au layers using an e-beam evaporator. The fabricated transistors were doped by OTS or APTES. Here, the thickness of the gate oxide (SiO_2) was 90 nm.

Electrical Characterization of OTS- or APTES-Doped TMD Electronic Devices: The fabricated transistor devices were electrically analyzed using an HP 4415A semiconductor parameter analyzer (I_D–V_D and I_D–V_G). The threshold voltage (V_{TH}), carrier concentration (n), and field-effect mobility (μ_{FE}) were calculated from the I_D–V_G data (Figure S4, Supporting Information). For these calculations, we used the following equations: $\mu_{FE} = L/(WV_DC_{OX}) \times (\partial I_D/\partial V_G)$ and n (or p) $= I_DL/qW\mu V_D$, where q is the electron charge, L and W are the length and width of the channel, respectively, and the gate oxide capacitance per unit area (C_{OX}) is $\varepsilon_{OX} \times \varepsilon_0/t_{OX}$. For the comparison with other doping studies performed on different numbers of TMD layers, the extracted 2D carrier concentration values were normalized by the number of TMD layers.

Optical Characterization of OTS- or APTES-Doped TMD Optoelectronic Devices: To investigate the optoelectronic characteristics of the fabricated OTS- or APTES-doped TMD optoelectronic devices, a current–voltage (I_D–V_G) measurement was performed under both dark and illuminated conditions. Here, we used a dot laser with wavelengths of 520, 655, 785, and 850 nm, where the optical power was about 5.8 mW cm^{-2}. In order to characterize and compare the TMD optoelectronic devices doped by OTS or APTES, the photoresponsivity (R) and detectivity (D^*) were calculated from the I_D–V_G curves (Figure S5, Supporting Information). R is I_{Photo}/P_{Light} and D^* is $(RA^{1/2})/(2eI_{Dark})^{1/2}$, where I_{Photo} is the generated photocurrent (I_{Laser_on}–I_{Laser_off}), P_{Light} is the total incident optical power, A is the effective area of the detector, e is the absolute value of an electron charge (1.6×10^{-19} C), and I_{Dark} is the dark current.

Supporting Information

Supporting Information is available from the Wiley Online Library or from the author.

Acknowledgements

D.-H.K. and M.-S.K. contributed equally to this work. This work was supported by the National Research Foundation of Korea (NRF) grant funded by the Korea government (MSIP) (No.2015R1A2A2A01002965).

Received: March 23, 2015
Revised: May 4, 2015
Published online: May 26, 2015

[1] S. Das, R. Gulotty, A. V. Sumant, A. Roelofs, *Nano Lett.* **2014**, *14*, 2861.
[2] J. Pu, Y. Yomogida, K.-K. Liu, L.-J. Li, Y. Iwasa, T. Takenobu, *Nano Lett.* **2012**, *8*, 4013.
[3] G.-H. Lee, Y.-J. Yu, X. Cui, N. Petrone, C.-H. Lee, M. S. Choi, D.-Y. Lee, C. Lee, W. J. Yoo, K. Watanabe, T. Taniguchi, C. Nuckolls, P. Kim, J. Hone, *ACS Nano* **2013**, *7*, 7931.
[4] H.-Y. Chang, S. Yang, J. Lee, L. Tao, W.-S. Hwang, D. Jena, N. Lu, D. Akinwande, *ACS Nano* **2013**, *7*, 5446.

[5] Q. Wang, K. Xu, Z. Wang, F. Wang, Y. Huang, M. Safdar, X. Zhan, F. Wang, Z. Cheng, J. He, *Nano Lett.* **2015**, *15*, 1183.
[6] K. F. Mak, C. Lee, J. Hone, J. Shan, T. F. Heinz, *Phys. Rev. Lett.* **2010**, *105*, 136805.
[7] A. Splendiani, L. Sun, Y. Zhang, T. Li, J. Kim, C.-Y. Chim, G. Galli, F. Wang, *Nano Lett.* **2010**, *10*, 1271.
[8] B. Radisavljevic, A. Radenovic, J. Brivio, V. Giacometti, A. Kis, *Nat. Nanotechnol.* **2011**, *6*, 147.
[9] H. Wang, L. Yu, Y.-H. Lee, Y. Shi, A. Hsu, M. L. Chin, L.-J. Li, M. Dubey, J. Kong, T. Palacios, *Nano Lett.* **2012**, *9*, 4674.
[10] S. Kim, A. Konar, W.-S. Hwang, J. H. Lee, J. Lee, J. Yang, C. Jung, H. Kim, J.-B. Yoo, J.-Y. Choi, Y. W. Jin, S. Y. Lee, D. Jena, W. Choi, K. Kim, *Nat. Commun.* **2012**, *3*, 1011.
[11] O. Lopez-Sanchez, D. Lembke, M. Kayci, A. Radenovic, A. Kis, *Nat. Nanotechnol.* **2013**, *8*, 497.
[12] H. S. Lee, S.-W. Min, Y.-G. Chang, M. K. Park, T. Nam, H. Kim, J. H. Kim, S. Ryu, S. Im, *Nano Lett.* **2012**, *12*, 3695.
[13] W. Choi, M. Y. Cho, A. Konar, J. H. Lee, G.-B. Cha, S. C. Hong, S. Kim, J. Kim, D. Jena, J. Joo, S. Kim, *Adv. Mater.* **2012**, *24*, 5832.
[14] M. Shanmugam, T. Bansal, C. A. Durcan, B. Yu, *Appl. Phys. Lett.* **2012**, *100*, 153901.
[15] M.-L. Tsai, S.-H. Su, J.-K. Chang, D.-S. Tsai, C.-H. Chen, C.-I. Wu, L.-J. Li, L.-J. Chen, J.-H. He, *ACS Nano* **2014**, *8*, 8317.
[16] J. Y. Yang, S. K. Kim, W. Choi, S. H. Park, Y. K. Jung, M. H. Cho, H. S. Kim, *ACS Appl. Mater. Interfaces* **2013**, *5*, 4739.
[17] Y. Li, C. Y. Xu, P. Hu, L. Zhen, *ACS Nano* **2013**, *7*, 7795.
[18] D.-H. Kang, J. Shim, S. K. Jang, J. Jeon, M. H. Jeon, G. Y. Yeom, W.-S. Jung, Y. H. Jang, S. Lee, J.-H. Park, *ACS Nano* **2015**, *9*, 1099.
[19] H. Y. Park, S. R. Dugasani, D.-H. Kang, J. Jeon, S. K. Jang, S. Lee, Y. Roh, S. H. Park, J.-H. Park, *ACS Nano* **2014**, *8*, 11603.
[20] J. D. Lin, C. Han, F. Wang, R. Wang, D. Xiang, S. Qin, X.-A. Zhang, L. Wang, H. Zhang, A. T. S. Wee, W. Chen, *ACS Nano* **2014**, *8*, 5323.
[21] S. Najmaei, X. Zou, D. Er, J. Li, Z. Jin, W. Gao, Q. Zhang, S. Park, L. Ge, S. Lei, J. Kono, V. B. Shenoy, B. I. Yakobson, A. George, P. M. Ajayan, J. Lou, *Nano Lett.* **2014**, *14*, 1354.
[22] A. M. Jones, H. Yu, N. J. Ghimire, S. Wu, G. Aivazian, J. S. Ross, B. Zhao, J. Yan, D. G. Mandrus, D. Xiao, W. Yao, X. Xu, *Nat. Nanotechnol.* **2013**, *8*, 634.
[23] J. S. Ross, P. Klement, A. M. Jones, N. J. Ghimire, J. Yan, D. G. Mandrus, T. Taniguchi, K. Watanabe, K. Kitamura, W. Yao, D. H. Cobden, X. Xu, *Nat. Nanotechnol.* **2014**, *9*, 268.
[24] N. Alidoust, G. Bian, S.-Y. Xu, R. Sankar, M. Neupane, C. Liu, I. Belopolski, D.-X. Qu, J. D. Denlinger, F.-C. Chou, M. Z. Hasan, *Nat. Commun.* **2013**, *5*, 4673.
[25] K. F. Mak, K. He, C. Lee, G. H. Lee, J. Hone, T. F. Heinz, J. Shan, *Nat. Mater.* **2012**, *12*, 207.
[26] K. He, N. Kumar, L. Zhao, Z. Wang, K. F. Mak, H. Zhao, J. Shan, *Phys. Rev. Lett.* **2014**, *113*, 026803.
[27] Z. Li, S.-W. Chang, C.-C. Chen, S. B. Cronin, *Nano Res.* **2014**, *7*, 973.
[28] K. Roy, M. Padmanabhan, S. Goswami, T. P. Sai, G. Ramalingam, S. Raghavan, A. Ghosh, *Nat. Nanotechnol.* **2013**, *8*, 826.
[29] Y. Li, C.-Y. Xu, J.-Y. Wang, L. Zhen, *Sci. Rep.* **2014**, *4*, 7186.
[30] V. Patil, A. Capone, S. Strauf, E.-H. Yang, *Sci. Rep.* **2013**, *3*, 2791.
[31] S. H. Yu, Y. Lee, S. K. Jang, J. Kang, J. Jeon, C. Lee, J. Y. Lee, H. Kim, E. Hwang, S. Lee, J. H. Cho, *ACS Nano* **2014**, *8*, 8285.
[32] O. Seitz, P. G. Fernandes, R. Tian, N. Karnik, H.-C. Wen, H. Stiegler, R. A. Chapman, E. M. Vogel, Y. J. Chabal, *J. Mater. Chem.* **2011**, *21*, 4384.